INSTITUTE OF PHYSICS PUBLISHING JOURNAL OF MICROMECHANICS AND MICROENGINEERING

J. Micromech. Microeng. **16** (2006) 242–253 doi:10.1088/0960-1317/16/2/008

A thermal actuator for nanoscale *in situ* microscopy testing: design and characterization

Yong Zhu, Alberto Corigliano[1] and Horacio D Espinosa

Department of Mechanical Engineering, Northwestern University, 2145 Sheridan Road, Evanston, IL 60208-3111, USA

E-mail: espinosa@northwestern.edu

Received 30 June 2005, in final form 16 November 2005
Published 5 January 2006
Online at stacks.iop.org/JMM/16/242

Abstract

This paper addresses the design and optimization of thermal actuators employed in a novel MEMS-based material testing system. The testing system is designed to measure the mechanical properties of a variety of materials/structures from thin films to one-dimensional structures, e.g. carbon nanotubes (CNTs) and nanowires (NWs). It includes a thermal actuator and a capacitive load sensor with a specimen in-between. The thermal actuator consists of a number of V-shaped beams anchored at both ends. It is capable of generating tens of milli-Newton force and a few micrometers displacement depending on the beams' angle and their number. Analytical expressions of the actuator thermomechanical response are derived and discussed. From these expressions, a number of design criteria are drawn and used to optimize the device response. The analytical predictions are compared with both finite element multiphysics analysis (FEA) and experiments. To demonstrate the actuator performance, polysilicon freestanding specimens cofabricated with the testing system are tested.

(Some figures in this article are in colour only in the electronic version)

1. Introduction

Nanostructures including nanotubes and nanowires have demonstrated great potential in a variety of applications ranging from nanocomposites to nanoelectromechanical systems (NEMS). It is therefore of particular relevance to accurately evaluate the mechanical properties of such nanostructures. This task is quite challenging in view of their nanometer size scale and requirements in terms of load and displacement resolution. Existing techniques for measuring mechanical properties of thin films usually cannot be applied to this purpose. Hence, novel nanoscale material testing systems are required. Microelectromechanical systems (MEMS) offer a promising class of actuators and sensors that can be used in building such material testing systems. In particular, thermal actuation appears quite promising.

Thermal actuation has been demonstrated as a compact, stable and high-force actuation technique [7] with some advantages over electrostatic actuation. Thermal actuators have been employed in a variety of applications: linear and rotary microengines [17], 2D nanoscale positioners [4], optical benches [16] and instrumentation for material property characterization [10]. Thermal actuators have also been integrated with compliant mechanisms to increase their displacement range for certain applications [4].

Thermal actuation is based on electric, thermal and structural-coupled fields. Recent efforts on modeling thermal actuators have focused on two approaches: sequential electrothermal and thermostructural analyses [3, 9, 12] and fully coupled three-dimensional (3D) finite element analysis (FEA) [14]. In addition, other efforts have been made on characterizing temperature-dependent electrothermal properties [7, 13], which is essential to the overall thermal actuator simulation.

[1] On leave from the Department of Structural Engineering, Politecnico di Milano, piazza Leonardo da Vinci 32, 20133 Milano, Italy.

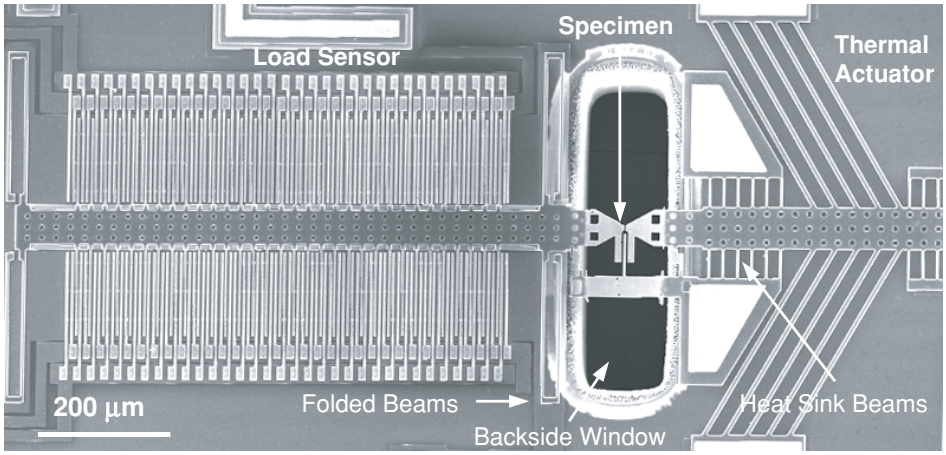

Figure 1. A MEMS-based material testing system consisting of a thermal actuator, a load sensor and a specimen.

This paper describes a thermal actuator used in a novel MEMS-based material testing system developed by Zhu and Espinosa [20]. The material testing systems were fabricated using the multi-user MEMS process (MUMPs) (MEMSCAP, Durham, NC) and they have been successfully operated *in situ* scanning and transmission electron microscopes (SEM and TEM). Here, analytical expressions of the thermal actuator response are derived following a structural mechanics approach. In addition, 3D FEA multiphysics simulations were performed to obtain full quantification of the field variables including the temperature distribution in the device. Design criteria in accordance with the requirements of testing various nanostructures are then drawn. Comparison between simulations, analytical formulas and experiments are pursued to interrogate and calibrate the device. In particular, we demonstrate the device performance by means of the testing of freestanding polysilicon specimens.

2. Device description

A MEMS-based material testing system designed for nanoscale tensile testing of nano-objects is shown in figure 1. The whole device is made of three components: a *thermal actuator*, a *specimen* and a *load sensor*. The system shown in figure 1 is specifically designed for *in situ* TEM testing. As such a backside window through the wafer under the specimen is etched in the final stages of the device microfabrication. Details on the device microfabrication are given in [21]. The SEM version of the device is easier to microfabricate because it does not require such a window (see [22]).

A schematic representation of the thermal actuator, first component of the device, is shown in figure 2: five pairs of inclined beams are clamped to the substrate and to the freestanding central shuttle, which can be considered as rigid in a first approximation of the structure. When a voltage difference is applied across the two anchor sites, heat is generated along the beams due to ohmic dissipation. The generated increase in the temperature in turn expands the beams and moves the shuttle in the direction shown in figure 2 [18]. A number of thermal sink beams, visible in figure 1, are placed near the specimen to minimize specimen heating.

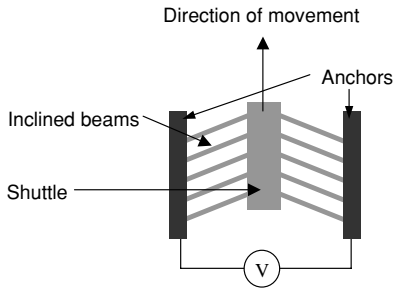

Figure 2. Schematic of the thermal actuator.

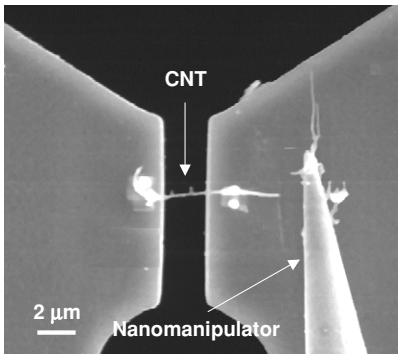

Figure 3. SEM image of the MEMS device with a carbon nanotube (CNT) specimen mounted by nanomanipulation [20].

The second component of the device shown in figure 1 is the specimen to be tested under tensile loading. The present device has been conceived to allow tensile testing of different materials/structures at the nanoscale. One such application, discussed in section 5, concerns with the tensile testing of polysilicon films, cofabricated with the device. Other specimens, such as CNTs and NWs, were mounted across a gap fabricated between the actuator and the load sensor, by means of nanomanipulation [20]. Figure 3 shows an example of a CNT mounted on the device in such a fashion.

The third component of the device is the capacitive load sensor. It consists of a number of parallel plate differential capacitors (figure 1), which are used to measure the displacement of the shuttle to which they are rigidly connected. Since the specimen and the load sensor are placed in series, the load acting on the specimen equals that on the folded beams (load sensor suspension springs). A resonance method is used to measure the elastic stiffness of the folded beams. With the known stiffness and the displacement of the load sensor shuttle, the load in the specimen is therefore obtained. A detailed description of the design and operation of the load sensor is given in [22].

Several issues concerning the actuator behavior are discussed in the following sections: the linear mechanical behavior of the actuator for a given temperature increase along the beams including optimization of the device during the design phase (section 3); the temperature distribution in the inclined beams and in the central shuttle in vacuum (section 4) and other features of the actuator such as buckling of the inclined beams and damage due to excessive heating (sections 3 and 4).

3. Analytical modeling

Analysis of a thermal actuator requires a coupled electric, thermal and mechanical investigation. In this section, the mechanical behavior of the device is analytically derived on the basis of the following assumptions: the average temperature increase in the inclined beams of the thermal actuator is known; the central shuttle is rigid and not affected by the temperature increase; small strains and displacements are considered and the shear deformation of the beams is negligible, i.e. an infinite shear stiffness is assumed.

This section starts with the description of the behavior of a single pair of inclined beams in the actuator (section 3.1), followed by that of the whole device including the thermal actuator, the specimen and the load sensor (section 3.2). Section 3.3 discusses critical buckling conditions and finally, section 3.4 draws a number of design criteria based on the above analyses.

3.1. Thermomechanical response of a pair of inclined beams

The basic constituent of the thermal actuator is a pair of inclined beams connected between the substrate and the central rigid shuttle. The system is schematically illustrated in figure 4(*a*) as a V-shaped clamped beam subject to a uniform increase in temperature along its length. Thermomechanical response of a similar structure was derived following a simplified beam analysis considering second-order effects of lateral bending [8]; here we analyze this problem considering both lateral bending and axial deformation of the beams under a small deformation hypothesis.

The mechanical response of the structure in figure 4(*a*) can be equivalently computed by considering half of the structure, as shown in figure 4(*b*); details are given in appendix.

The displacement at node A in the *y*-direction and the reaction force in the *x*-direction, due to an average temperature

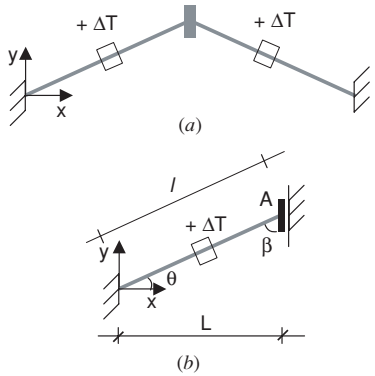

Figure 4. Schematic of a pair of inclined beams subjected to an average increase in temperature ΔT: (*a*) two beams joint at the central shuttle and (*b*) equivalent mechanical representation of a single beam.

increase of ΔT along the beam, are given in the following, respectively:

$$U^{\Delta T} \equiv U_y^{\mathrm{A}} = \alpha \Delta T l \frac{s}{\left(s^2 + c^2 \frac{12I}{Al^2}\right)} \equiv \alpha \Delta T l \frac{s}{\left(s^2 + \frac{c^2}{\psi}\right)}, \tag{1a}$$

$$R_x^{\Delta T} \equiv R_x^{\mathrm{A}} = -\alpha \Delta T\, EA \frac{c}{\left(s^2 \frac{Al^2}{12I} + c^2\right)} \equiv -\alpha \Delta T\, EA \frac{c}{(s^2 \psi + c^2)} \tag{1b}$$

where α is the coefficient of thermal expansion of the beam material, E is Young's modulus of the material, l is the beam length, A is the beam cross section, I is the moment of inertia of the cross section with respect to the out of plane axis z and c and s are cosine and sine of the beam angle θ as defined in figure 4(*b*). The dimensionless parameter $\psi = Al^2/12I$ is defined as the axial over bending stiffness ratio.

The displacement at node A due to an external force F applied to the central shuttle along the y-direction is (see appendix)

$$U^F \equiv U_y^{\mathrm{A}} = F \frac{1}{2\left(s^2 \frac{EA}{l} + c^2 \frac{12EI}{l^3}\right)} = \frac{Fl}{EA} \frac{1}{2\left(s^2 + \frac{c^2}{\psi}\right)}. \tag{2}$$

The ratio $K_{\mathrm{tb}} \equiv F/U^F = 2\left(s^2 + \frac{c^2}{\psi}\right) EA/l$ represents the stiffness of the V-shaped clamped thermal beam of figure 4(*a*).

In the case that the V-shaped thermal beam is subjected to both a temperature increase ΔT and an external force F, the displacement is (equations (1*a*) and (2))

$$U^{\Delta T+F} = U^{\Delta T} + U^F = (2\alpha \Delta T\, EAs + F)/K_{\mathrm{tb}}. \tag{3}$$

As mentioned in the preceding section, a number of heat *sink beams* are placed near the specimen to reduce the influence of the actuator temperature on the specimen. For one pair of heat sink beams, the stiffness in the shuttle-moving direction is

$$K_{\mathrm{sb}} = 2 \times \frac{12EI_{\mathrm{sb}}}{l_{\mathrm{sb}}^3} = \frac{2Eb_{\mathrm{sb}}^3 h}{l_{\mathrm{sb}}^3}, \tag{4}$$

where I_{sb}, l_{sb} and b_{sb} are the moment of inertia, length and width of the sink beams, respectively.

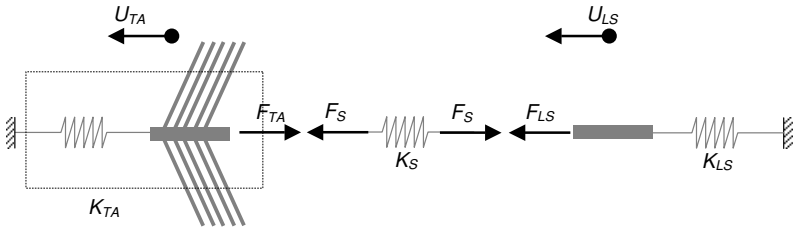

Figure 5. Lumped model of the device with internal forces and displacements shown in a free body diagram representation.

Consider the thermal actuator consisting of m pairs of thermal beams and n pairs of heat sink beams, its stiffness and displacement are given, respectively, as

$$K_{\mathrm{TA}} = mK_{\mathrm{tb}} + nK_{\mathrm{sb}} \tag{5a}$$

$$U_{\mathrm{TA}} = (U^{\Delta T} mK_{\mathrm{tb}} + F)/K_{\mathrm{TA}} = (2m\alpha\Delta T\, EAs + F)/K_{\mathrm{TA}}, \tag{5b}$$

where $U^{\Delta T}$ is the displacement of the thermal actuator without sink beams, as given by equation (1*a*). Relation (5*b*) is obtained by imposing kinematics compatibility to the systems of thermal beams and sink beams.

3.2. Thermomechanical response of the whole device

Having computed the mechanical response of the actuator due to thermal loading, as shown in figure 4, it is now possible to obtain the equations governing the behavior of the whole device. The lumped model used for the mechanical analysis is shown in figure 5, where the elastic stiffness of the specimen is denoted by K_{S}, the elastic stiffness of the load sensor, coinciding with the elastic stiffness of the folded beams to which it is suspended, is denoted by K_{LS} and the displacement of the load sensor is denoted by U_{LS}. Note that the central shuttle of the load sensor is assumed to be rigid. In figure 5, K_{TA} is the elastic stiffness of the thermal actuator, as computed in section 3.1 (equation (5*a*)).

The governing equations of the lumped system, with positive forces as shown in figure 5, are given by

$$\begin{aligned}
\Delta U_{\mathrm{S}} &= U_{\mathrm{TA}} - U_{\mathrm{LS}} \\
U_{\mathrm{TA}} &= (U^{\Delta T} mK_{\mathrm{tb}} - F_{\mathrm{TA}})/K_{\mathrm{TA}} \\
&= (2m\alpha\Delta T\, EAs - F_{\mathrm{TA}})/K_{\mathrm{TA}} \\
F_{\mathrm{TA}} &= F_{\mathrm{S}} = F_{\mathrm{LS}} \\
F_{\mathrm{S}} &= K_{\mathrm{S}}\Delta U_{\mathrm{S}} \\
F_{\mathrm{LS}} &= K_{\mathrm{LS}} U_{\mathrm{LS}},
\end{aligned} \tag{6}$$

where ΔU_{S} is the elongation of the specimen. Solving the governing relations (6) we obtain the displacement of the thermal actuator U_{TA}, the force in the specimen F_{S}, the elongation of the specimen ΔU_{S} and the displacement of the load sensor U_{LS}, namely,

$$\begin{aligned}
U_{\mathrm{TA}} &= \frac{2m\alpha\Delta T\, EAs}{(K_{\mathrm{TA}} + K_{\mathrm{TA}}K_{\mathrm{LS}}/K_{\mathrm{S}} + K_{\mathrm{LS}})} \\
&\quad + \frac{2m\alpha\Delta T\, EAs}{(K_{\mathrm{TA}} + K_{\mathrm{S}} + K_{\mathrm{TA}}K_{\mathrm{S}}/K_{\mathrm{LS}})} \\
F_{\mathrm{S}} &= \frac{2m\alpha\Delta T\, EAs}{(K_{\mathrm{TA}}/K_{\mathrm{S}} + 1 + K_{\mathrm{TA}}/K_{\mathrm{LS}})} \\
\Delta U_{\mathrm{S}} &= \frac{2m\alpha\Delta T\, EAs}{(K_{\mathrm{TA}} + K_{\mathrm{S}} + K_{\mathrm{TA}}K_{\mathrm{S}}/K_{\mathrm{LS}})} \\
U_{\mathrm{LS}} &= \frac{2m\alpha\Delta T\, EAs}{(K_{\mathrm{TA}} + K_{\mathrm{TA}}K_{\mathrm{LS}}/K_{\mathrm{S}} + K_{\mathrm{LS}})}.
\end{aligned} \tag{7}$$

3.3. Buckling analysis

It is important to estimate under what conditions the inclined beams might buckle. Buckling occurs when the internal force exceeds the critical buckling force. Based on the device geometry, figure 1, the boundary conditions for the beam are: the anchor is fixed while the other end, connected to the shuttle, cannot rotate but it can translate, figure 4(*b*).

Buckling occurs in the plane where the moment of inertia is minimum. It can be orthogonal to or parallel to the substrate depending on the beam dimensions. The critical force for buckling can then be written as

$$P_{\mathrm{cr}} = \pi^2 \frac{EI_{\min}}{l^2}. \tag{8}$$

When the thermal actuator is disconnected from the specimen and the heat sink beams, the axial internal force in the thermal beams is compressive and given by $R_x^{\Delta T} c = \alpha\Delta T\, EA \frac{c^2}{(s^2\psi + c^2)}$, where $R_x^{\Delta T}$ is given by equation (1*b*). When the thermal actuator is connected to the specimen, heat sink beams and the load sensor, the maximum value of the axial internal force that can theoretically be achieved is $\alpha\Delta T\, EA$, i.e. when the actuator shuttle cannot translate (thermal actuator is connected to an elastic system with infinite stiffness). The actual axial force in the beams has a magnitude between these two extremes.

3.4. Design criteria

To achieve an effective and reliable material testing system, we need to meet several design goals:

1. large load sensor displacements in order to increase the load resolution;
2. low temperature at the actuator–specimen interface;
3. the testing system operates in displacement control, i.e. the thermal actuator stiffness is much higher than the stiffness of the specimen and load sensor and
4. the thermal actuator does not buckle within the operational temperature range.

The choice of actuator geometry, number of inclined beams and their dimensions, and of K_{LS} is a strong function

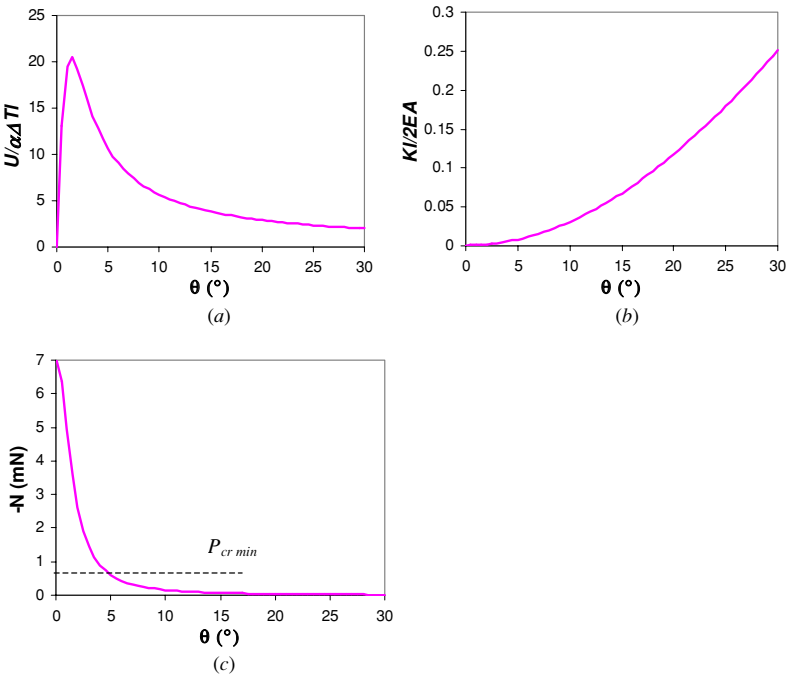

Figure 6. Important parameters in the device design as functions of the thermal beam angle: (*a*) displacement; (*b*) stiffness of the thermal actuator and (*c*) internal stress. The parameters in (*a*) and (*b*) are plotted as dimensionless quantities. In the *y*-axis of (*b*), K is K_{tb}, the stiffness of the V-shaped clamped thermal beam of figure 4(*a*).

of the specimen stiffness, failure load and elongation at failure (ΔU_{S}). Hence, device optimization requires some preliminary knowledge of the specimen behavior as customary in experimental mechanics. In relation to the choice of load sensor stiffness (K_{LS}), the smaller it is, the larger the load sensor displacement (U_{LS}) is. The force applied to the specimen is measured as $F_{\mathrm{S}} = F_{\mathrm{LS}} = K_{\mathrm{LS}}U_{\mathrm{LS}}$. Note that for the differential capacitance load sensor, the displacement resolution is approximately constant [22], we infer that the smaller K_{LS} is, the higher the load resolution. However, in order to achieve a given ΔU_{S}, the thermal actuator displacement (U_{TA}) must also increase (see equation (6*a*)). In the extreme case of $K_{\mathrm{LS}} = 0$, i.e. when the load sensor is not fixed to the substrate by folded beams, $U_{\mathrm{TA}} = U_{\mathrm{LS}}$ and the specimen translate rigidly, without elongation.

From equation (1), it is seen that the displacement of the thermal actuator when unconstrained by sink beams and disconnected to the specimen depends on the beam length (l), the beam angle (θ), the temperature increase and stiffness ratio ψ. Hence, the longer the beams the larger the displacement. However, note that longer beams are more likely to undergo stiction during the microfabrication process and buckling. Therefore, there is a practical limit to the inclined beam length. In our design, the beam length is selected as 300 μm.

Figure 6(*a*) shows the thermal actuator displacement given by equation (1*a*) as a function of the beam angle. Here the displacement is plotted as a dimensionless quantity ($U^{\Delta T}/\alpha\Delta T l$) for a fixed stiffness ratio $\psi = 1406$. It is seen that the displacement increases with the decrease of the beam angle in the range $\theta > 2^{\circ}$. In other words, in order to obtain the same displacement, the actuator with a smaller beam angle (in the range $\theta > 2^{\circ}$) requires a lower temperature increase or equivalently a lower actuation voltage.

In relation to the third design criterion mentioned above, it is desirable to have the thermal actuator operating in a displacement control mode. Displacement control is critical in mechanical testing because it is capable of capturing some important mechanical phenomena, such as stress softening and fracture. In order to achieve displacement control, ideally the actuator should possess an infinite stiffness. In practice, the actuator stiffness needs to be much larger than that of the specimen and of the load sensor. Figure 6(*b*) plots the actuator stiffness as a function of the beam angle for a fixed stiffness ratio $\psi = 1406$. Note that stiffness is plotted as a dimensionless quantity ($K_{\mathrm{tb}}l/2EA$). In contrast to the displacement angular dependence, the plot shows that the actuator stiffness increases with the beam angle. Hence, the selection of beam angle is a trade off between desired maximum displacement and stiffness.

The last design criterion deals with the possibility of beam buckling. When the temperature increases in the beams, the internal force increases and beam buckling may occur. For the given beam dimensions (e.g. beam length $l = 300$ μm, beam width $b = 8$ μm and beam height $h = 3.5$ μm), the minimum buckling force (0.532 mN) occurs in the plane perpendicular to the substrate. Figure 6(*c*) plots the internal force, as a function of the beam angle and the minimum buckling force, for a temperature increase $\Delta T = 800$ K. Since the polysilicon recrystallization temperature is roughly 800 K [6], buckling is not expected within the functional temperature of the actuator. From the plot it is observed that at 800 K, the actuator buckles when the beam angle is less than approximately 5°.

In summary, the actuator with a small beam angle requires the lowest temperature increase to achieve a given displacement; however, its structural stability decreases. For

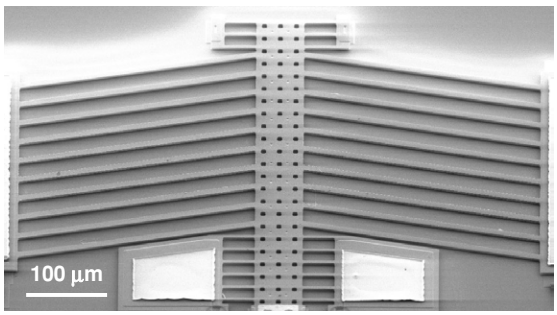

(*a*)

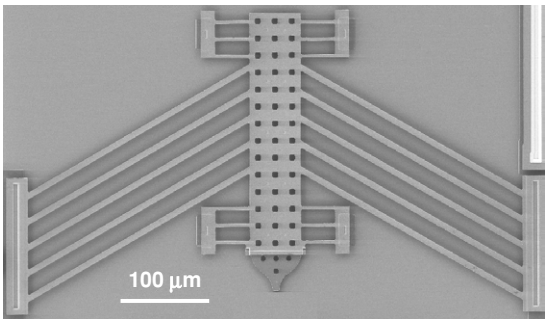

(*b*)

Figure 7. Two types of thermal actuators for testing various types of nanostructures: (*a*) ten pairs of thermal beams with a beam angle of 10° and (*b*) five pairs of thermal beams with a beam angle of 30°.

the selected beam dimensions, the beam angle needs to be larger than about 5° to avoid buckling. Considering a safety factor of two, the beam angle cannot be smaller than about 10°. Following these criteria, two types of beam angles were selected to test various nanostructures: 10° for those that require large thermal actuator displacement (figure 7(*a*)) and 30° for those that require moderate thermal actuator displacement (figure 7(*b*)). The number of thermal beams can be adjusted to achieve the desired actuator stiffness/load sensor stiffness and actuator stiffness/specimen stiffness ratios. Likewise, the load sensor stiffness must be selected according to equations (6) and (7) once an estimate of the specimen stiffness and elongation at failure has been made.

Multiphysics analysis will be performed in the subsequent section to provide an assessment of the temperature at the specimen–actuator interface and to examine the effectiveness of heat sink beams in controlling temperature increase in the specimen.

4. Multiphysics FEA

When the device is operated in air, the major heat dissipation mechanism is heat transfer between the device and the substrate through the air gap. By contrast, in vacuum, the dominant heat dissipation mechanism is heat conduction to the substrate through the anchors. Since the device discussed in this paper is intended to operate inside the SEM and TEM, an electrothermal analysis in vacuum is conducted. For details on electrothermal analysis of a thermal actuator, refer to [9].

The performance of the thermal actuator in vacuum is simulated using the finite element software ANSYS multiphysics, version 6.1. The simulation is a coupled-field analysis involving electric, thermal and mechanical fields. The input is the actuation voltage across the anchor sites and the output includes the actuator temperature and displacement fields. The thermal boundary conditions are zero temperature change at the anchors. The mechanical boundary conditions are fixed displacements at the anchor sites. The polysilicon parameters used in the simulation are listed in table 1. The displacement of the actuator in vacuum can be obtained experimentally; however, it is difficult to measure the temperature distribution. Therefore, the coupled-field simulation is particularly relevant to provide such information.

Figure 8 shows the temperature distribution and the displacement in the thermal actuator for an actuation voltage of 1 V. As previously stated, in vacuum the only heat dissipation path is through the anchors. Since the shuttle is the farthest from the anchors, the highest temperature occurs in the shuttle, as shown in figure 8(*a*). As a result of temperature nonuniformity, the displacement in the shuttle is also not uniform, figure 8(*b*).

An undesired feature of the thermal actuator is that the specimen temperature can be high due to heat conduction through the shuttle. This problem can be mitigated by placing a number of so-called heat sink beams close to the specimen, as shown in figures 1 and 9. The thermal actuator with 30° beam angle is used as an example to illustrate the effects of the heat sink beams on the temperature increase at the specimen–actuator interface. Figures 9(*a*) and (*b*) show the temperature increase and the displacement in the shuttle axial direction for the case of three pairs of sink beams, respectively. To prevent out-of-plane bending, another three pairs of beams are positioned at the other end of the shuttle. In the analyses, the heat sink beams are 40 μm long and 4 μm wide with 16 μm spacing. Compared to the case without sink

Table 1. Polysilicon properties used in the simulation of the thermal actuator.

Parameter	Unit	Value	Reference
Young's modulus	GPa	170	[19]
Poisson's ratio	–	0.22	[19]
Thermal conductivity	W m^{-1} K^{-1}	34	[3]
Resistivity (constant)	Ω m	3.4×10^{-5}	[12]
Resistivity (temperature dependent)	Ω m	$3.4 \times 10^{-5}[1 + 1.25 \times 10^{-3}(T - 293)]$	[12]
Thermal expansion coefficient (constant)	K^{-1}	2.5×10^{-6}	[7]
Thermal expansion coefficient (temperature dependent)	K^{-1}	$-4 \times 10^{-12}T^2 + 8 \times 10^{-9}T + 4 \times 10^{-7}$	[7]

Note: in the above equations, T should be provided in Kelvin.

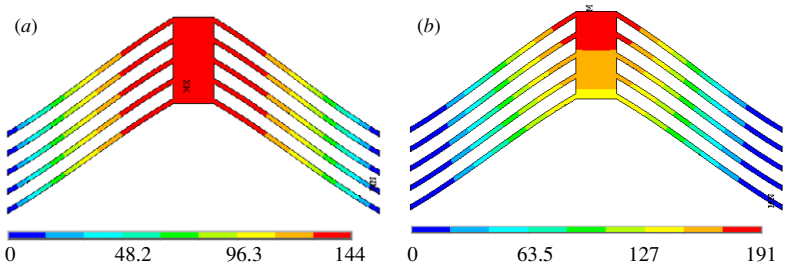

Figure 8. (*a*) Temperature increase field (in °C) and (*b*) displacement field (in nm) in the thermal actuator. The displacement component in the plot is in the shuttle axial direction.

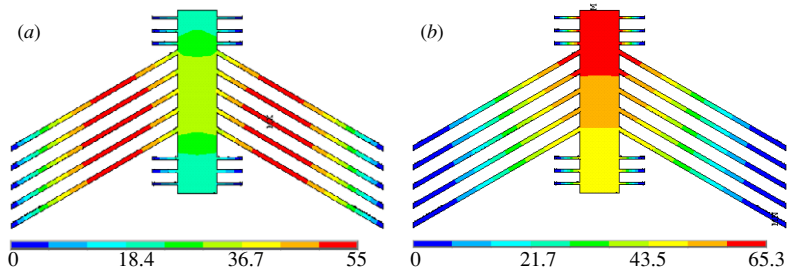

Figure 9. (*a*) Temperature (in °C) and (*b*) displacement (in nm) fields in the thermal actuator with three pairs of heat sink beams at the specimen end. The displacement component in the plot is in the shuttle axial direction.

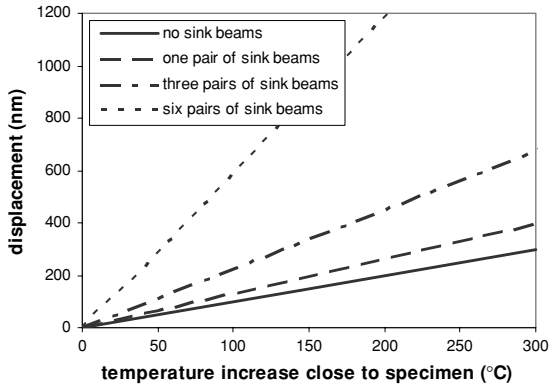

Figure 10. Displacement at the actuator–specimen interface as a function of temperature increase for various numbers of heat sink beams.

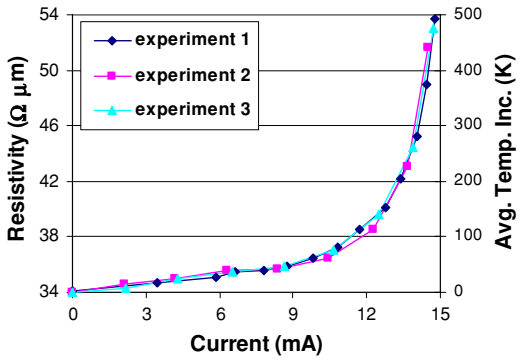

Figure 11. Electric resistivity and corresponding temperature increase as functions of the input current for three thermal actuators.

beams, the three pairs of sink beams configuration achieve over two times the displacement at the specimen end for the same allowable temperature increase at the specimen–actuator interface. When six pairs of sink beams are employed, the displacement is six times larger as shown in figure 10. If needed, the specimen heating problem can be additionally alleviated by introducing a thermal isolation layer between the actuator and the specimen following a custom microfabrication process [18].

In the section that follows, the temperature field numerically computed will be used in the experimental assessment of the device performance. Through comparison between numerical prediction and experimental measurements, we will examine the accuracy of the analytical predictions. We will also examine the accuracy of the predicted temperature field, a feature that is very important in view of the difficulties in its experimental measurement.

5. Experiments

The microfabricated thermal actuators were tested inside the SEM and TEM to assess their performance. The experimental setup employed in the test is described in [20]. In the experimental characterization of the actuator two variables are of particular relevance: (i) the average temperature increase in the freestanding inclined beams and (ii) the shuttle displacement, i.e. the prescribed displacement to the specimen. The tested actuators consisted of five pairs of inclined beams at 30° and three pairs of heat sink beams at each end. Three different actuators with identical dimensions, on the same die, were tested.

The average temperature increase in the actuator was estimated from the change in electric resistivity as the input current increased. In figure 11, the average resistivity and temperature increase are plotted as a function of current flow through the inclined beams. The average resistivity was obtained from measured resistance and inclined beam cross-sectional area. The temperature was then determined from

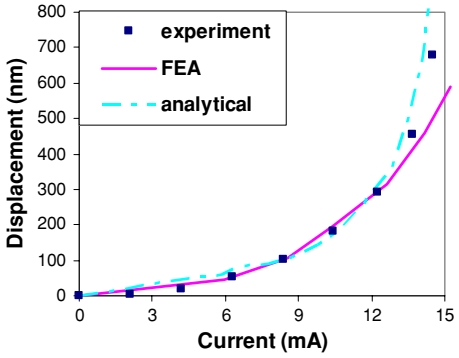

Figure 12. Displacement at the actuator–specimen interface as a function of the input current. Experiments, FEA and analytical expression show good agreement. The experimental result is the average of three experimental measurements obtained from geometrical identical thermal actuators. In the multiphysics analysis, a temperature-dependent thermal expansion coefficient was used; in the analytical expression, a constant thermal expansion coefficient was used (see table 1). The slight deviation at the high operational currents is probably due to inaccuracies in the physical parameters such as resistivity and thermal conductivity.

the resistivity–temperature relationship given in table 1. In figure 11, we report three experimental results as obtained from three devices with identical geometry. Nearly identical performances were measured, which shows that the device properties are quite uniform across the die.

Figure 12 shows the average measured displacement of the three actuators at the specimen ends. The average was performed over three measurements on identical devices. The displacement of the thermal actuator in the SEM was measured by the method described in [22], which provides a resolution of 5 nm or better. When the actuator is tested without a specimen, i.e. as an independent unit, displacements of approximately 800 nm were generated at a current of 15 mA. With the calculated stiffness of 54×10^3 N m^{-1}, the force necessary to reduce the displacements to zero is 43.2 mN. The calculated displacements using the analytically derived formula and the ANSYS multiphysics simulation are also plotted in figure 12. In the analytical prediction, the average temperature in the thermal actuator, obtained from the three experimental results reported in figure 11, was employed. Then the displacement was calculated based on the known thermal expansion coefficient. In the ANSYS simulation, voltage was applied at the anchors as previously discussed, and the temperature field was computed. Then, by computing the actuator resistance based on the resistivity for a computed average temperature, over the length of the five pairs of beams, the current was obtained. Examination of figure 12 reveals that the multiphysics numerical simulation exhibits a good agreement with the experimental measurements. The implication is that a multiphysics simulation can be employed to predict the actuator response, for any geometry, and to determine the average beam temperature increase needed in the analytical formulas. The slight deviation between the experiments and the simulation at large current is likely due to inaccuracies in the physical parameters such as resistivity and thermal conductivity at high temperature [7, 12]. We will also show next that the polysilicon microstructure is modified at current levels above 12 mA, starting point for the discrepancy.

Although it is difficult to directly measure temperature distribution within the SEM, we were able to detect the material microstructural change, due to Joule heating, when currents were above a certain threshold. Figure 13(*a*) shows an image of the thermal actuator at a current level of 12 mA. Due to symmetry, only half of the actuator was imaged. The location of highest temperature in the inclined beams is clearly seen in the SEM image. Figure 13(*b*) shows the temperature distribution obtained from FEA. The location of highest predicted temperature agrees very well with the experimental observation. Furthermore, we imaged the beams, at high magnification, at the location of highest temperature under various input currents. The images are shown in figure 14 for currents of 12 mA, 16 mA and 18 mA. It is known that as temperature increases beyond a threshold, polysilicon undergoes recrystallization and localized melting at the grain boundaries [12]. Figures 14(*a*)–(*c*) confirm this phenomenon. Three stages can be identified: normal working condition, recrystallization and localized melting at the grain boundaries.

Another important feature of the actuator is its out-of-plane displacement within the operational range. Keeping the material testing system free from out-of-plane motion is critical for accurate mechanical measurement of nanoscale objects. Out-of-plane motion may introduce undesired bending on the objects and spurious effects. The out-of-plane motion of the designed thermal actuator was examined in *air* using an optical profilometer with 2.2 nm vertical resolution (MicroXAM, ADE Phase Shift Technology). The load sensor, which was separated from the actuator by a gap, was used as a reference level. Two points were selected, one on the actuator and the other one on the load sensor. By comparing the z values of these two points, the out-of-plane motion of the actuator as a function of applied voltage was obtained. The out-of-plane motion as a function of the input current is plotted in figure 15. The input current range is much higher than that in *vacuum* because in air heat conduction to the substrate through the air gap occurs and as a result higher currents are needed to achieve the same temperature increase. Here the actuator shown in figure 7(*b*) was examined. A maximum displacement of 20 nm was measured, which shows the actuator possesses excellent stability in the out-of-plane direction.

6. Application: tensile testing of a polysilicon thin film specimen

In this section, we demonstrate the performance of the actuator by characterizing the constitutive response of polysilicon. Polysilicon was selected because its Young's modulus and strength are well characterized. Moreover, polysilicon films require failure forces that are not easily achievable with other actuation principles such as electrostatic actuation. The dog-bone-shaped specimen was nanomachined using a focused ion beam (FIB). The specimen dimensions in the constant strain region were: 6 μm long and 1.6 μm thick, see figure 16(*a*) inset. The cross section was trapezoidal with a 0.42 μm top width and a 1.04 μm bottom width. Two displacement markers, 4.7 μm apart, were deposited using

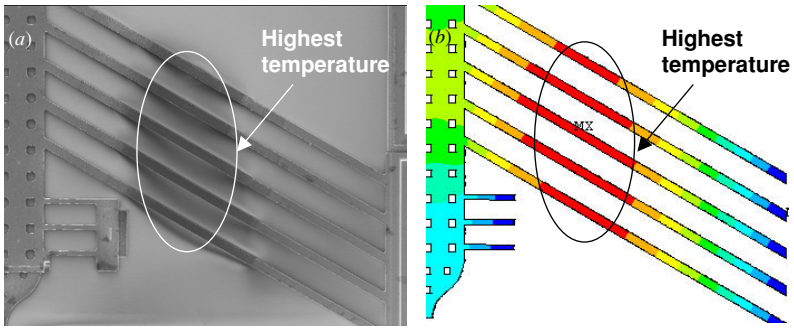

Figure 13. (*a*) A SEM image of half of the thermal actuator at an operational current of 12 mA. (*b*) The temperature distribution obtained from FEA. Due to symmetry, only half of the thermal actuator is shown.

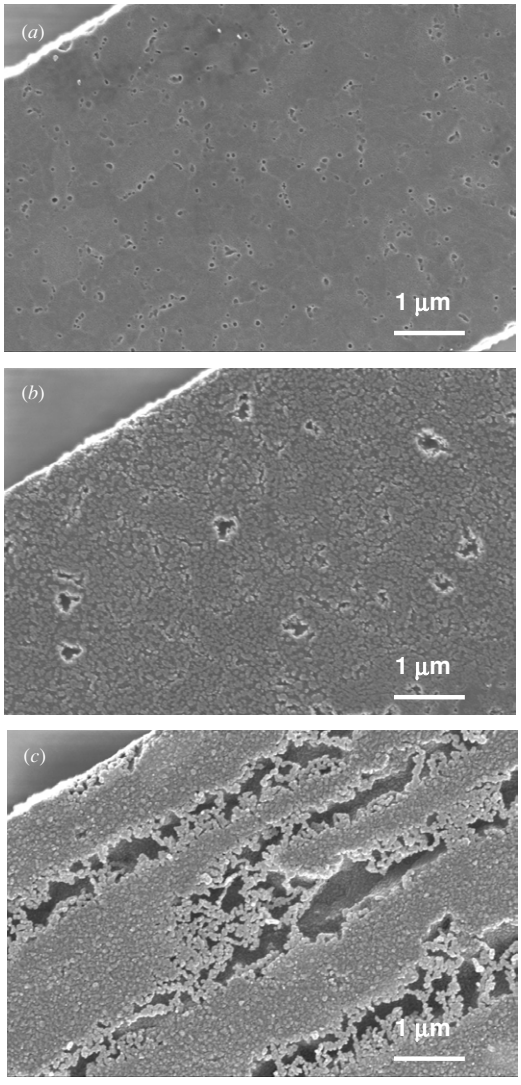

Figure 14. SEM images showing the thermal actuator at three current levels: (*a*) 12 mA, (*b*) 16 mA and (*c*) 18 mA. Three operational conditions can be identified: normal working condition, recrystallization and localized melting at the grain boundaries, respectively.

the electron beam-induced deposition of platinum. Assuming Young's modulus of 170 GPa, the stiffness of the specimen between the two displacement markers was computed to be

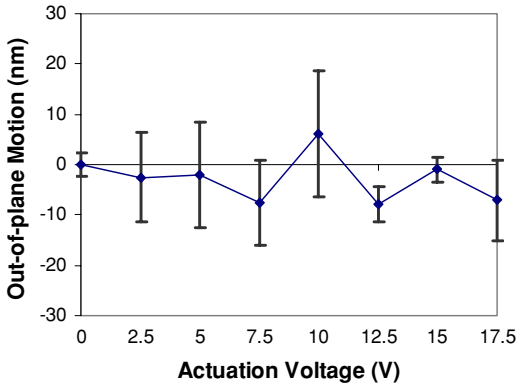

Figure 15. Out-of-plane motion of the thermal actuator as a function of current. The measurement was performed in air using an optical profilometer. Several measurements were performed at each current level. The range of the measurements is shown in the plot.

42×10^3 N m^{-1}. Moreover, assuming a rupture strain of 1% [1, 19], the elongation at rupture between the two markers was estimated to be 47 nm. Following the governing equations given in section 3.2, we designed the load sensor to be supported by two stiff folded beams at the specimen end, beam stiffness of 3020 N m^{-1}, as shown in figure 16(*a*). In this case, the load sensor was expected to move 655 nm just prior to specimen failure. The capacitive load sensor calibration methodology reported by Zhu *et al* [22] was employed to interpret the experiments.

During the experiment, the specimen elongation between the markers just prior to specimen failure was measured as 43 ± 5 nm, and the load sensor moved 548 ± 1 nm as recorded by the capacitance measurement. The failure strain was about $(0.91 \pm 0.1)\%$, which is very close to the assumed value of 1%. The failure force was calculated to be 1.655 ± 0.003 mN and the failure strength was 1417 ± 3 MPa. The calculated stress–strain curve is shown in figure 16(*b*). The Young modulus was found to be 156 ± 17 GPa. The stress–strain curve is linear up to failure, which is typical of brittle material failure. These results agree well with the literature-reported values for polysilicon [2, 5, 19].

The actuator displacement at the specimen end is approximately the sum of the load sensor motion and the specimen elongation. From figure 10, we estimate the temperature increase at the specimen end to be about 130 °C.

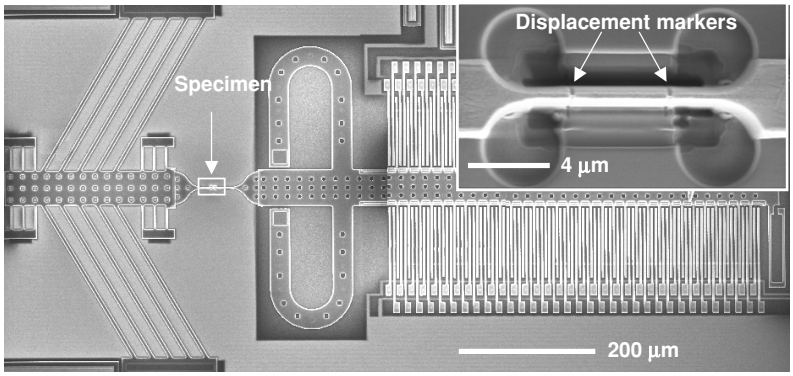

(*a*)

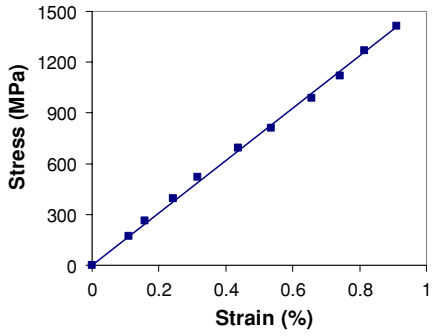

(*b*)

Figure 16. Quantitative *in situ* SEM test of a freestanding polysilicon film. (*a*) Entire testing system including thermal actuator, load sensor and freestanding polysilicon film in-between. Inset at the top right corner shows the dog-bone-shaped specimen with two displacement markers. Note that the load sensor was supported by very stiff folded beams at the sample end. (*b*) Stress–strain behavior of the polysilicon specimen.

The thermal strain in the sample is then calculated to be 0.03% based on the thermal expansion coefficient given in table 1. The corrected tensile strain at failure is then 0.88%. It is therefore inferred that the error on the computed value of Young's modulus is mainly due to the inaccuracy in the strain measurement. Nonetheless, if the actuator calibration based on the multiphysics analysis of the device is employed, the error due to thermal strain can be removed. In the cases of NWs and CNTs, the actuator displacement is generally less than 100 nm [21]. As a result, the actuator temperature increase is expected to be lower than 20 °C according to figure 10. Consequently, the temperature effect in determining the Young modulus of nano-objects is expected to be negligible.

7. Conclusions

This paper examined the performance of a thermal actuator for MEMS-based material testing with particular emphasis on its design and calibration. The resulting compact testing system can be easily placed inside a SEM chamber or a TEM holder for *in situ* mechanical testing. The thermal actuator was modeled both analytically and by coupled-field FEA. The beam angle was identified as an important parameter in maximizing the actuator displacement at a given applied voltage (temperature increase). Following several design criteria, 10° and 30° beam angles were selected for the purpose of testing various types of materials/structures. Numerical analysis confirmed that the temperature at the actuator–specimen interface can be controlled by adding a number of heat sink beams. Experimental measurements of displacement agree very well with the FEA predictions. In addition, the average temperature increase obtained from the resistivity measurement is consistent with the FEA results. Hence, the numerical predictions allow determination of the average temperature increase in the actuator. Furthermore, when this average temperature is input in the analytical formulas, the computed displacement agrees very well with the value measured experimentally.

To demonstrate the capability of the testing system, freestanding polysilicon films were tested. The measured Young modulus and failure strength were in good agreement with those reported in the literature. This confirms that the thermal actuator can be employed advantageously in nanoscale material characterization. Displacement control is achieved by the thermal actuation, in contrast to the electrostatic actuation which is force control. Displacement control is a very important feature in the characterization of inelasticity and damage.

An important remark is on the direct temperature measurement of the thermal actuator. Until recently the most commonly used temperature measurement technique was infrared thermography, which is limited in spatial resolution and susceptible to variations in emissivity which requires extensive calibration. Raman scattering in combination with optical microscopy offers a much improved spatial resolution

of 1 μm or better and more accurate temperature measurement without the need for extensive calibration measurements [11]. Although this is able to provide important information on the temperature distribution in the ambient, an additional challenge must be overcome to achieve the temperature measurement inside SEM.

Acknowledgments

This project is supported by the National Science Foundation under award no. DMR-0315561. Characterization of the thermal actuators in SEM was performed at the Electron Probe Instrumentation Center at Northwestern University. A Corigliano is grateful for the financial support of the Department of Mechanical Engineering at Northwestern University.

Appendix

In order to find the displacement of node A (figure 4(*b*)) in the *y*-direction and the axial force in the beam, it is sufficient to assemble the elastic stiffness matrix of the beam relevant to the displacements of node A. To obtain this matrix in the global frame of figure 4(*b*), we first compute the elastic stiffness matrix in a local reference frame, as shown in figure A1. The system of equations governing the structural behavior of the beam, when subjected to the average increase in temperature ΔT, is

$$\begin{bmatrix} \frac{EA}{l} & 0 \\ 0 & \frac{12EI}{l^3} \end{bmatrix} \begin{bmatrix} U_\xi^{\mathrm{A}} \\ U_\eta^{\mathrm{A}} \end{bmatrix} = \begin{bmatrix} \alpha\, \Delta T\, EA \\ 0 \end{bmatrix} + \begin{bmatrix} R_\xi^{\mathrm{A}} \\ R_\eta^{\mathrm{A}} \end{bmatrix}, \tag{A1}$$

where A is the beam cross section, l is the beam length, E is Young's modulus of the beam material, I is the moment of inertia of the cross section with respect to the out-of-plane axis ζ in the local reference frame, U_ξ^{A} and U_η^{A} are the displacements of node A in the ξ and η directions, respectively, α is the coefficient of thermal expansion of the beam material, R_ξ^{A} and R_η^{A} are the reaction forces at node A in the ξ and η directions, respectively. Note that ξ and η represent the orthogonal directions in a local coordinate system as shown in figure A1.

In order to apply the boundary conditions in the global reference frame x–y of figure 4, the system (A1) is transformed by means of a rotation matrix relating the local degrees of freedom to the global ones, namely,

$$\begin{bmatrix} U_\xi^{\mathrm{A}} \\ U_\eta^{\mathrm{A}} \end{bmatrix} = \begin{bmatrix} \cos\theta & \sin\theta \\ -\sin\theta & \cos\theta \end{bmatrix} \begin{bmatrix} U_x^{\mathrm{A}} \\ U_y^{\mathrm{A}} \end{bmatrix} \equiv \begin{bmatrix} c & s \\ -s & c \end{bmatrix} \begin{bmatrix} U_x^{\mathrm{A}} \\ U_y^{\mathrm{A}} \end{bmatrix}, \tag{A2}$$

where U_x^{A} and U_y^{A} are the displacements of node A in the x and y directions, respectively.

By applying relation (A2), the system of equations (A1) transforms to

$$\begin{bmatrix} \left(c^2 \frac{EA}{l} + s^2 \frac{12EI}{l^3}\right) & cs\left(\frac{EA}{l} - \frac{12EI}{l^3}\right) \\ cs\left(\frac{EA}{l} - \frac{12EI}{l^3}\right) & \left(s^2 \frac{EA}{l} + c^2 \frac{12EI}{l^3}\right) \end{bmatrix} \begin{bmatrix} U_x^{\mathrm{A}} \\ U_y^{\mathrm{A}} \end{bmatrix} = \begin{bmatrix} \alpha \Delta T\, EAc \\ \alpha \Delta T\, EAs \end{bmatrix} + \begin{bmatrix} R_x^{\mathrm{A}} \\ R_y^{\mathrm{A}} \end{bmatrix}. \tag{A3}$$

Finally, the boundary conditions, which represent the constraint at node A in figure 4(*b*), are

$$U_x^{\mathrm{A}} = 0, \qquad R_x^{\mathrm{A}} \neq 0; \qquad U_y^{\mathrm{A}} \neq 0, \qquad R_y^{\mathrm{A}} = 0, \tag{A4}$$

where R_x^{A} and R_y^{A} are the reaction forces of node A in the x and y directions, respectively.

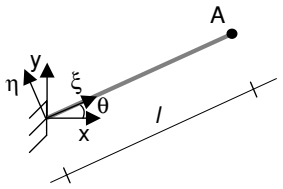

Figure A1. Schematic of an inclined beam in a local reference frame.

Substitution into the governing system of equations (A3) yields

$$\begin{bmatrix} \left(c^2 \frac{AE}{l} + s^2 \frac{12EI}{l^3}\right) & cs\left(\frac{AE}{l} - \frac{12EI}{l^3}\right) \\ cs\left(\frac{AE}{l} - \frac{12EI}{l^3}\right) & \left(s^2 \frac{AE}{l} + c^2 \frac{12EI}{l^3}\right) \end{bmatrix} \begin{bmatrix} 0 \\ U_y^{\mathrm{A}} \end{bmatrix} = \begin{bmatrix} \alpha \Delta T\, EAc \\ \alpha \Delta T\, EAs \end{bmatrix} + \begin{bmatrix} R_x^{\mathrm{A}} \\ 0 \end{bmatrix}. \tag{A5}$$

The second equation (A5) gives the displacement of node A in the y-direction due to an average increase in temperature ΔT along the beam, while the first equation provides the reaction force in the x-direction, namely,

$$\begin{aligned} U^{\Delta T} &\equiv U_y^{\mathrm{A}} = \alpha \Delta T\, l \frac{s}{\left(s^2 + c^2 \frac{12I}{Al^2}\right)} \\ &\equiv \alpha \Delta T\, l \frac{s}{\left(s^2 + \frac{c^2}{\psi}\right)} \\ R_x^{\Delta T} &\equiv R_x^{\mathrm{A}} = -\alpha \Delta T\, EA \frac{c}{\left(s^2 \frac{Al^2}{12I} + c^2\right)} \\ &\equiv -\alpha \Delta T\, EA \frac{c}{(s^2 \psi + c^2)}. \end{aligned} \tag{A6}$$

From the reaction R_x^{A}, it is possible to obtain the compressive axial internal force N in the beam by projection along the axial direction, namely, $N = R_x^{\mathrm{A}} c$. The dimensionless parameter $\psi = Al^2/12I$ is defined as the axial over bending stiffness ratio.

The response of a couple of inclined beams subject to an external force F, applied to the central shuttle and acting in the y-direction, can be obtained similarly. The solution in terms of the displacement of point A and axial internal force can be obtained starting from the governing system of equations (A5) where the vector depending on the temperature increase on the right side is substituted with the external force vector $[0\ F/2]^T$. Then we obtain

$$\begin{aligned} U^F &\equiv U_y^{\mathrm{A}} = F \frac{1}{2\left(s^2 \frac{EA}{l} + c^2 \frac{12EI}{l^3}\right)} = \frac{Fl}{EA} \frac{1}{2\left(s^2 + \frac{c^2}{\psi}\right)}, \\ R_x^F &\equiv R_x^{\mathrm{A}} = cs\left(\frac{EA}{l} - \frac{12EI}{l^3}\right) U_y^{\mathrm{A}} = F \frac{cs(\psi - 1)}{2(s^2 \psi + c^2)}. \end{aligned} \tag{A7}$$

References

[1] Chasiotis I and Knauss W G 2002 A new microtensile tester for the study of MEMS materials with the aid of atomic force microscopy *Exp. Mech.* **42** 51–7

[2] Chasiotis I and Knauss W G 2003 The mechanical strength of polysilicon films: Part 1. The influence of fabrication governed surface conditions *J. Mech. Phys. Solids* **51** 1533–50
[3] Chiao M and Lin L 2000 Self-buckling of micromachined beams under resistive heating *J. Microelectromech. Syst.* **9** 146–51
[4] Chu L L and Gianchandani Y B 2003 A micromachined 2D positioner with electrothermal actuation and sub-nanometer capacitive sensing *J. Micromech. Microeng.* **13** 279–85
[5] Corigliano A, Masi B D, Frangi A, Comi C, Villa A and Marchi M 2004 Mechanical characterization of polysilicon through on-chip tensile tests *J. Microelectromech. Syst.* **13** 200–19
[6] Ehmann M, Ruther P, von Arx M and Paul O 2001 Operation and short-term drift of polysilicon-heated CMOS microstructures at temperatures up to 1200 K *J. Micromech. Microeng.* **11** 397–401
[7] Geisberger A A, Sarkar N, Ellis M and Skidmore G 2003 Electrothermal properties and modeling of polysilicon microthermal actuators *J. Microelectromech. Syst.* **12** 513–23
[8] Gianchandani Y B and Najafi K 1996 Bent-beam strain sensors *J. Microelectromech. Syst.* **5** 52–8
[9] Huang Q and Lee N 1999 Analysis and design of polysilicon thermal flexure actuator *J. Micromech. Microeng.* **9** 64–70
[10] Kapels H, Aigner R and Binder J 2000 Fracture strength and fatigue of polysilicon determined by a novel thermal actuator *IEEE Trans. Electron Devices* **47** 1522–8
[11] Kuball M, Hayes J M, Uren M J, Martin I, Birbeck J C H, Balmer R S and Hughes B T 2002 Measurement of temperature in active high-power AlGaN/GaN HFETS using Raman spectroscopy *IEEE Electron Device Lett.* **23** 7–9
[12] Lott C D, Mc Lain T W, Harb J N and Howell L L 2002 Modeling the thermal behavior of a surface-micromachined linear-displacement thermomechanical microactuator *Sensors Actuators* A **101** 239–50
[13] Manginell R P 1997 A polysilicon microbridge gas sensor *PhD Thesis* University of New Mexico
[14] Mankame N D and Ananthasuresh G K 2001 Comprehensive thermal modeling and characterization of an electro-thermal-compliant microactuator *J. Micromech. Microeng.* **11** 452–62
[15] MUMPs web, http://www.memsrus.com/
[16] Pai M and Tien N C 2000 Low voltage electrothermal vibromotor for silicon optical bench applications *Sensors Actuators* A **83** 237–43
[17] Park J S, Chu L L, Oliver A D and Gianchandani Y B 2001 Bent-beam electrothermal actuators—Part II. linear and rotary microengines *J. Microelectromech. Syst.* **10** 255–62
[18] Que L, Park J S and Gianchandani Y B 2001 Bent-beam electrothermal actuators—Part I. Single beam and cascaded devices *J. Microelectromech. Syst.* **10** 247–54
[19] Sharpe W N Jr, Jackson K M, Hemker K J and Xie Z 2001 Effect of specimen size on Young's modulus and fracture strength of polysilicon *J. Microelectromech. Syst.* **10** 317–26
[20] Zhu Y and Espinosa H D 2005a An electro-mechanical material testing system for *in situ* electron microscopy and applications *Proc. Natl Acad. Sci. USA* **102** 14503–8
[21] Zhu Y and Espinosa H D 2005b Design and operation of a MEMS-based material testing system for *in situ* electron microscopy testing of nanostructures *J. Microelectromech. Syst.* submitted
[22] Zhu Y, Moldovan N and Espinosa H D 2005 A microelectromechanical load sensor for *in situ* electron and x-ray microscopy tensile testing of nanostructures *Appl. Phys. Lett.* **86** 013506